Image and Vision Computing 93 (2020) 103810

Contents lists available at ScienceDirect

Image and Vision Computing

journal homepage: www.elsevier.com/locate/imavis

Region-based Fitting of Overlapping Ellipses and its application to cells segmentation ☆

Costas Panagiotakis[a,c,*], Antonis Argyros[b,c]

[a] Management Science and Technology Department, Hellenic Mediterranean University, Agios Nikolaos 72100, Crete, Greece
[b] Computer Science Department, University of Crete, Heraklion 70013, Crete, Greece
[c] Institute of Computer Science, FORTH, Heraklion 70013, Crete, Greece

ARTICLE INFO

Article history:
Received 8 January 2019
Received in revised form 10 September 2019
Accepted 12 September 2019
Available online 31 October 2019

Keywords:
Cell segmentation
2D shape modeling
Overlapping objects
Ellipse fitting
AIC

ABSTRACT

We present RFOVE, a region-based method for approximating an arbitrary 2D shape with an automatically determined number of possibly overlapping ellipses. RFOVE is completely unsupervised, operates without any assumption or prior knowledge on the object's shape and extends and improves the Decremental Ellipse Fitting Algorithm (DEFA) [1]. Both RFOVE and DEFA solve the multi-ellipse fitting problem by performing model selection that is guided by the minimization of the Akaike Information Criterion on a suitably defined shape complexity measure. However, in contrast to DEFA, RFOVE minimizes an objective function that allows for ellipses with higher degree of overlap and, thus, achieves better ellipse-based shape approximation. A comparative evaluation of RFOVE with DEFA on several standard datasets shows that RFOVE achieves better shape coverage with simpler models (less ellipses). As a practical exploitation of RFOVE, we present its application to the problem of detecting and segmenting potentially overlapping cells in fluorescence microscopy images. Quantitative results obtained in three public datasets (one synthetic and two with more than 4000 actual stained cells) show the superiority of RFOVE over the state of the art in overlapping cells segmentation.

1. Introduction

The approximation of a 2D object with a sufficient number of geometric primitives is an interesting problem in computer vision and pattern recognition with several applications including object detection and retrieval [2,3], tracking [4], motion analysis and action recognition [5,6]. The selection of the type of prototypes such as rigid templates, line segments [7], deformable part models [8], circles [9,10], ellipses [1,11-15], ellipsoids and superquadrics [16,17] is application-dependent [1].

In our previous work [1], we have proposed the Augmentative Ellipse Fitting Algorithm (AEFA) and the Decremental Ellipse Fitting Algorithm (DEFA) to solve the problem of approximating a 2D shape by a set of ellipses. AEFA gradually increases the number of ellipses that approximate a given 2D shape starting from a single one, while DEFA reduces the number of ellipses starting with a large (but automatically determined) number of such ellipses. On average, DEFA is three times faster than AEFA and yields slightly better results [1]. Thus, in this work, we focus on improving DEFA.

DEFA approximates a 2D shape with an automatically determined number of ellipses, achieving a good balance between model complexity (number of ellipses) and shape coverage (percentage of shape points covered by the ellipses) under the so-called *Equal Area constraint*. According to this constraint, the sum of the areas of all ellipses should be equal to the area of the given shape. The parameters of the ellipses are iteratively estimated based on the covariance matrix of the shape pixels that are associated to them through *hard clustering*. Due to this hard clustering, DEFA gives good quality solutions when the shape can be approximated with ellipses of low overlap. However, in case that the shape is better approximated with considerably overlapping ellipses, DEFA fails to estimate accurately their parameters. In this work, we overcome this problem by relaxing the Equal Area constraint and by optimizing directly for shape coverage. More specifically, we require that the union of shape points under all estimated ellipses is as close as possible to the area of the original shape. This allows a data point to be associated with more than one ellipses and makes a very significant difference in the final result.

☆ This paper has been recommended for acceptance by S. Todorovic.

* Corresponding author at: Management Science and Technology Department, Hellenic Mediterranean University, Agios Nikolaos 72100, Crete, Greece.
E-mail addresses: cpanag@ics.forth.gr (C. Panagiotakis), argyros@ics.forth.gr (A. Argyros).

https://doi.org/10.1016/j.imavis.2019.09.001
0262-8856/

Fig. 1 (a), (b) and (c) show the results of DEFA and RFOVE in a simple, illustrative example of a shape that consists of two overlapping ellipses. DEFA gives a coverage of 94.2% with two ellipses (Fig. 1 (a)) and of 95.1% with one ellipse (Fig. 1 (b)), and selects one ellipse to represent this shape. RFOVE (Fig. 1 (c)) gives a coverage of 99.1% with two ellipses. Clearly, the solution of RFOVE agrees better with human intuition. The yellow points in Fig. 1 (c) contribute to the estimation of both ellipses.

Fig. 1 (d) shows several overlapping 2D elliptical shapes and the result of the application of RFOVE. The ground truth centroid of each object is shown with a red plus. The boundaries detected by the proposed method are plotted in green color and are in almost full agreement with the ground truth.

The superiority of RFOVE over DEFA has been experimentally verified in several public datasets. On top of this, we assess the impact of RFOVE on the problem of cell segmentation in fluorescence microscopy images. Cell segmentation plays a key role in high-throughput applications such as quantification of protein expression and the study of cell function [19]. Moreover, the detection of overlapping objects of different size and pose that do not usually contain enough visible geometrical evidence, make cell boundary estimation a very challenging task [18]. Fig. 1 (e) shows a fluorescence microscopy image of cells that are heterogeneous in shape and size. The image exhibits considerable foreground and background intensity variations. In Fig. 1 (f) the ground truth centroid of each cell is shown with a red plus. The boundaries detected by RFOVE are plotted in green color and are in almost full agreement with the ground truth, despite the existence of several touching/overlapping cells.

2. Related work

We review representative research efforts related to the problem of ellipse-based approximation of a given 2D shape as well as to the problem of cell segmentation.

2.1. Approximating 2D shapes with ellipses

Several methods have been proposed for modeling a given 2D shape with a set of ellipses. Most of them can be classified into (a) boundary-based methods that minimize the approximation error between the ellipses and edge data points and (b) region-based methods that minimize the approximation error between the regions of ellipses and the given shape [1]. The first category of methods typically employ the Hough Transform [20], Genetic Algorithms [21] or edge-following schemes [22]. Most of them work well when the ellipses are partially occluded, but cannot perform region-based fitting of multiple ellipses. Other methods fit ellipses based on the detection of special geometric points e.g. pupils in the case of faces images [11], that are used to define three main parameters of the ellipses (ellipse center, orientation, minor and major axis).

Region based methods are more tolerant to noise since they take into account all shape points. For a single ellipse, its parameters can be analytically determined based on the second order moments of the data [5]. For more than one ellipses, several methods provide approximate solutions. For some approaches, the number of ellipses should be known a priori [23]. Other methods assume that other aspects of the model structure is known [24]. As an example, in [24] a Gaussian Mixture Model (GMM) is estimated using Expectation-Maximization (EM) for decomposing a silhouette into images. This method assumes a known number of ellipses which must be organized in a known hierarchical structure. These two constraints greatly simplify the problem because they permit the optimization of a subset of ellipses at a time as opposed to the optimization of the full set of parameters of an unknown number of ellipses. In [25], the 2D skeleton of a shape is used to partition it into a set of regions. Then, a set of ellipses is computed for each region via least squares fitting. A greedy cost minimization is then applied to the entire model to merge any suboptimal ellipses in a way that maximizes the coverage of the 2D shape. The use of a 2D skeleton and the local ellipse fitting

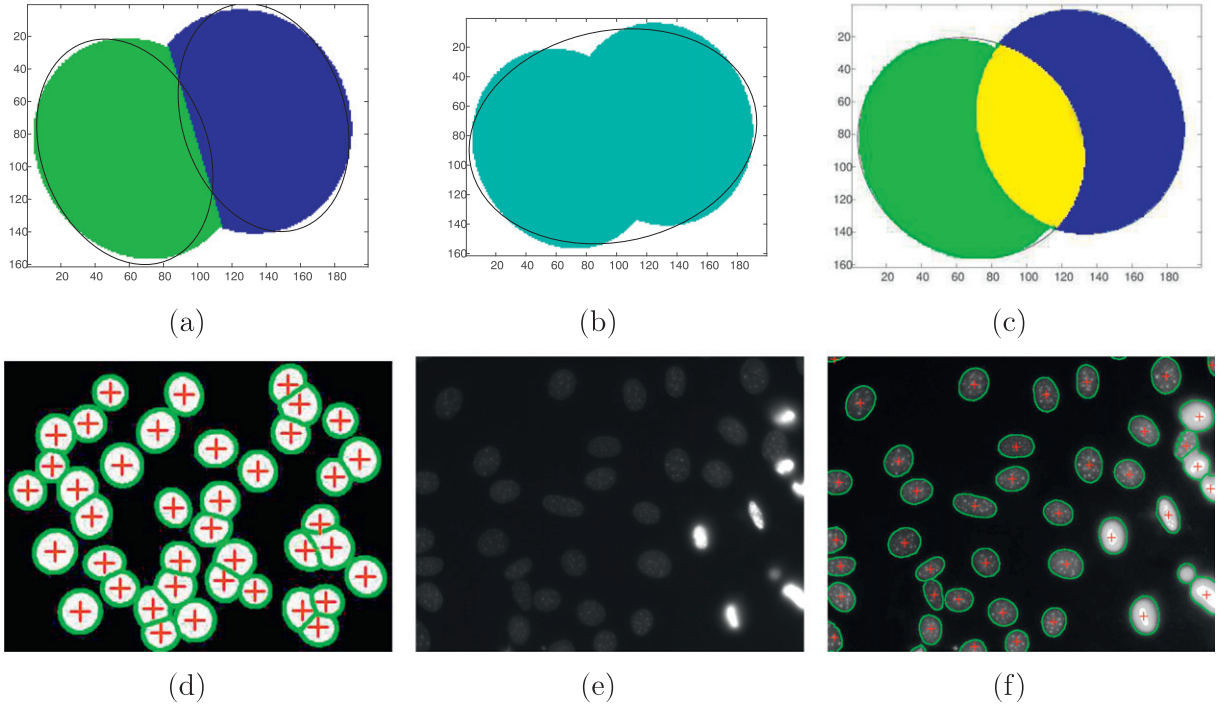

Fig. 1. (a) The green and blue points constitute the foreground. The figure shows the results of DEFA when forced to estimate two ellipses. The two colors indicate the achieved assignment of points to ellipses. (b) DEFA result for the image of (a) when DEFA estimates a single ellipse. (c) The result from the application of the proposed RFOVE algorithm on the same data. The yellow points participate in the estimation on both ellipses. (d) The result of RFOVE in a synthetic image from [18]. (e) A fluorescence microscopy image and (f) the output of the proposed method. In (d) and (f) the boundaries of the detected objects are shown in green color and their ground truth centroids are plotted as red pluses. (For interpretation of the references to color in this figure legend, the reader is referred to the web version of this article.)

makes this method very fast. However, it is sensitive to errors occurring during the initial selection of regions. For example, the use of 2D skeleton failed to accurately detect the borders between regions of different width (e.g., see Fig. 3 (b) of [25]).

2.2. Cell segmentation

Image segmentation is a key step in many image/video analysis tasks and multimedia applications [26]. Cell segmentation is an important problem in biomedical image analysis, which we use as a benchmark for assessing the usefulness of the proposed RFOVE method. Cell segmentation can be addressed by interactive techniques [27]. However, interactive/manual cell segmentation is a subjective, tedious, labor-intensive and time-consuming task, especially for large datasets. Therefore, automatic cell segmentation methods with the ability to deal with different cell types and image artifacts are required [19,18,12].

Several image segmentation methods have been proposed to automatically detect and split overlapping cells in fluorescence microscopy images. Most of these methods consist of two major steps, (a) segmenting cells and cell constellations from their image background and (b) splitting of overlapping cells. One popular thresholding method that can be used as an initialization step in cell detection is Otsu's method [12-14,28,29], that performs fully automatic, clustering-based image thresholding. Otsu's method calculates the optimum threshold separating the foreground from the background so that their combined spread (intra-class variance) is minimal. The Otsu's method does not perform sufficiently well when the assumption of a bimodal image intensities distribution is violated. This happens, for example, when there is considerable intensity inhomogeneity in the image foreground and/or background (e.g., see Fig. 1 (e)). This problem is also common to other segmentation methods that compute global thresholds for detecting cells [30].

Deformable models, which are able to capture a wide spectrum of shapes, can also be considered as another category of cell segmentation techniques [19]. There are two main types of deformable models: parametric, which use an explicit representation of objects, and implicit like level sets. Level sets methods [31,32,12] have been used to extract contours and to evaluate whether a cell is blurry. Such methods show promising results, but they usually require initialization e.g., by Otsu's method as proposed in [12].

Deep convolutional neural networks (CNNs) have been applied recently to cell segmentation [33-35], cell splitting [36] and tracking [37] so as to learn cell appearance features. In [33], a deep CNN is combined with the Voronoi diagram of clusters to detect neutrophils, a primary type of immune cells. The CNN-based hierarchical representation of features outperforms hand-crafted features on this task. In [35], cell segmentation is performed using MultiResUNet architecture, a modified version of U-Net [38], that improves the results of the state-of-the-art U-Net model[38]. In [34], a multistage CNN is trained to produce the categorization of all pixels. Deep CNNs have been also applied to the problem of cell nuclei splitting [36], yielding high performance results even when the training set is a small subset of the original dataset. In [37], the proposed cell tracking method consists of a particle filter motion model, a multi-task learning observation model based on CNNs, and an optimized model update strategy to enable the multi-task observation model for the variation of the tracked cell over the entire tracking procedure. Such methods yield high performance results, but are training set dependent.

The splitting of touching cells is often handled with watershed-based segmentation [39,40]. However, such methods suffer from over-segmentation when cells have different sizes and shapes [13]. The over-segmentation is reduced in [40] using marker-controlled watersheds, but the detection of markers is still not accurate in cases of considerably overlapping cells [12]. In [19], touching cells are first distinguished from non-touching ones based on predefined rules applied to the convex hull of the segmented cell regions. Then, splitting is achieved by identifying splitting point-pairs. In [30] the splitting is performed by minimizing the maximum eccentricity of the resulting sub-regions under the constraint of equal cells area. This results in equally sized cells of almost circular shape.

Many recent methods [12-15] operate by fitting ellipses to the boundaries of segmented cells, or to specific proper boundary split points. In [14] and [15], the problem of overlapping objects segmentation is treated by first identifying concave points through polygonal approximation. The concave points in the objects contour are used to identify splitting points on the contours. Finally, ellipse fitting is applied to such splitting points to separate the overlapping objects. Similarly, in [13], a cell image is segmented by thresholding, followed by a polygonal approximation to extract the feature points of cell contours. Then, candidate splitting point pairs are obtained by calculating the bottleneck rate of point pairs and then by using ellipse fitting to identify the correct splitting point pair. Another recent method that follows this approach is presented in [12] and consists of four steps: contour extraction, concave point detection, contour segment grouping and ellipse fitting. The concave points include corner points of a cell which are detected by applying a number of empirical criteria. A basic rule for contour segment grouping is that if two segments are connected and split by one concave point, they should not belong to the same group. Finally, an ellipse is fitted to each group using least squares fitting [41]. Ellipses with minor and major axes of appropriate length and low least squares fitting error are preserved. These methods give satisfactory results, however, they are sensitive to errors on boundary detection and they rely on heuristically determined thresholds to identify the splitting points of the touching cells.

In [42,18], two boundary-based methods have been proposed that use seed point extraction to discriminate overlapping objects. The seed point extraction methods recognize the presence and estimate the number of the individual objects in the image as identified by the seed points [18]. In [42], a modified erosion process is used for decomposing a mixture of particles into markers, and then an edge-to-marker association method is proposed to identify the set of evidences that eventually delineate individual objects. Next, the set of evidences is input to a Gaussian mixture model on B-splines, the solution of which leads to the joint learning of the missing contour and the particle shape. In [18], a method starts with seed point extraction using bounded erosion and Fast Radial Symmetry transform (FRS) [43]. FRS is a feature extraction technique that transforms the original image to a new representation that highlights the local radial symmetry of the image gradient. Extracted seed points are then utilized to associate edge points to objects in order to create contour evidence. Finally, the contours of the objects are estimated by fitting ellipses to the contour evidence. Curvature estimation can be also used for cell splitting [13,14,44], but such methods share the aforementioned robustness issues that are common to the rest of the boundary-based methods. Another seed point extraction method is the Slide Band Filter (SBF) method [45], which belongs to the family of local convergence filters. SBF estimates the overall convergence by combining all the individual convergence degrees of sample points in such way that the convergence of the pixel interest point is maximized along each radial direction.

In a recent work [46], we applied DEFA for the cell segmentation problem, yielding promising results when the touching cells have low ratios of overlap. In this work, we employ the proposed RFOVE method to solve the cell segmentation problem yielding high performance results even when the cells overlap ratio is high. Similarly with [46], we employ a modified version of the Bradley's segmentation method [47], which is a real-time adaptive thresholding using the mean of a local window to improve the accuracy in cell detection. The Bradley's method is selected because it is local and adaptive and performs well in challenging images with intensity inhomogeneity.

By employing the same baseline cell segmentation strategy as in [46] and replacing DEFA with RFOVE, we show the impact of RFOVE in a practical and important vision and pattern recognition problem.

2.3. Our contribution

In summary, the main contributions of this paper are:

- RFOVE an efficient, region based, parameter-free method for approximating a 2D shape with ellipses.
- The experimental, quantitative evaluation of RFOVE based on several standard datasets which reveals its state of the art performance.
- The use of RFOVE to solve the problem of segmenting and splitting cells in fluorescence microscopy images.
- The experimental evaluation of RFOVE-based cell segmentation on standard datasets, which reveals its state of the art performance in comparison to DEFA and several other existing methods.

3. RFOVE: Region-based Fitting of Overlapping Ellipses

We present the proposed method for Region-based Fitting of Overlapping Ellipses (RFOVE) that improves and extends the multi-ellipse fitting method (DEFA) [1]. Similarly to DEFA, RFOVE approximates an arbitrary 2D shape with a number of ellipses, without any assumption or prior knowledge regarding the input shape.

3.1. Problem formulation

We assume a binary image I that represents a 2D shape. A pixel p of I belongs either to the foreground F ($I(p) = 1$) or to the background B ($I(p) = 0$). The area A of the 2D shape is given by

$$A = \sum_{p \in F} I(p). \tag{1}$$

We also assume a set E of k ellipses E_i, each with individual area $|E_i|$. A binary image U_E is also defined so that $U_E(p) = 1$ at points p that are inside any of the ellipses E_i and $U_E(p) = 0$, otherwise. Then, we define the coverage α_E of the 2D shape by the given set of ellipses E as:

$$\alpha_E = \frac{1}{A} \sum_{p \in F} I(p) U_E(p). \tag{2}$$

Essentially, α_E is the percentage of the 2D shape points that are under some of the ellipses in E.

Let $|E|$ denote the sum of the areas of all ellipses $|E| = \sum_{i=1}^{k} |E_i|$. Let C_E denote the area covered by all ellipses:

$$C_E = \sum_{p \in I} U_E(p). \tag{3}$$

It should be stressed that $C_E \leq |E|$, with the equality holding in the case that all ellipses are pairwise disjoint. This is because in case of two overlapping ellipses, $|E|$ counts the area of their intersection two times, while C_E does not.

DEFA [1] estimates the parameters of a set $E*$ of k ellipses E_i^* so that α_{E^*} as defined in Eq. (2) is maximized under the *Equal Area constraint*. According to this constraint, it should hold that $|E*| = A$. Instead, in RFOVE we want to maximize the shape coverage α_{E^*} with a set of ellipses $E*$ whose C_{E^*} is as close as possible to A. In notation,

$$E^* = \arg\max_{E} \alpha_E \quad s.t. \quad C_E = A. \tag{4}$$

In order to estimate the optimal number k of ellipses, we optimize the trade-off between shape coverage α_E and model complexity (number of ellipses) by employing the Akaike Information Criterion (AIC) [48] on the shape complexity measure C defined in [1]. This is computed on the basis of the radii of the circles that are centered on the 2D skeleton of the shape and are maximally inscribed in it. The AIC-based model selection criterion amounts to the minimization of the quantity [1]

$$AIC(E, C) = Cln(1 - \alpha_E) + 2k, \tag{5}$$

over all possible numbers of ellipses, k. Intuitively, this achieves a good balance between the increased shape coverage that is achieved as more ellipses are used to approximate a certain shape, with the associated increased complexity of that model (due to the increase of the number of employed ellipses).

The shape complexity measure we use as well as the model selection process are invariant to shape rotation and translation and are slightly affected by scale changes, mainly due to quantization/resolution issues.

3.2. The RFOVE algorithm

RFOVE operates similarly to DEFA and in a number of steps which are summarized as follows.

3.2.1. Skeleton extraction

First, the medial axis (skeleton) S of the 2D shape is computed, which provides important information on the parameters of the ellipses that could approximate the original shape. Medial axis skeletonization is sensitive to minor boundary deformations, in the sense that a small perturbation of the boundary of a shape may result in a significant skeleton branch. To alleviate this problem, instead of medial axis-based skeletonization we employ shape thinning [49] combined with a closing morphological filter [50].

3.2.2. Initialization of ellipse hypotheses

RFOVE defines a set CC of circles that are used as initial ellipse hypotheses. The centers of these circles lie on S and their radii are defined by the minimum distance of these centers from the contour of the shape. Circles are considered for inclusion in CC in decreasing order with respect to their radius. Initially, $CC = \emptyset$. Each considered circle is introduced in CC if its overlap with the already selected circles is below a certain threshold. In order to reduce the cardinality of CC and the complexity of RFOVE, circles with radius lower than 3% of the maximum radius are ignored. The number of initial circle hypotheses constitutes an upper bound for the maximum number of fitting ellipses.

3.2.3. Evolution of ellipse hypotheses

The Gaussian Mixture Model Expectation Maximization (GMM-EM) algorithm is responsible for computing the parameters of a fixed number k of the ellipses in E with the best coverage α_E of the given 2D shape. This is achieved by repeatedly applying two steps (a) shape points assignment to ellipses, and (b) ellipse parameters estimation.

- *Assignment of shape points to ellipses:* A point p is assigned to an ellipse E_i iff p is inside that ellipse. Formally, it should hold that

$$F(p, E_i) \leq 1.0, \tag{6}$$

where

$$F(p, E_i) = \frac{||p - c_i||}{||p' - c_i||}. \tag{7}$$

In Eq. (7), c_i is the origin of ellipse E_i, p' is the intersection of the line connecting p and c_i with the ellipse E_i, and $||\cdot||$ signifies the length of a 2D vector. Thus, $F(p, E_i) = 1.0$ for points p that lie on the boundary of E_i. Given that ellipses may overlap, a shape point p may be associated with more than one ellipses.

- *Estimation of ellipse parameters:* The parameters of an ellipse E_i are directly updated by the second order moments of the points associated to this ellipse in the previous, assignment step.

3.2.4. Solving for the optimal number of ellipses

Different models (i.e., solutions involving different numbers of ellipses) are evaluated based on the AIC criterion (see Eq. (5)) that balances the trade off between model complexity and approximation error. In order to minimize the AIC criterion, RFOVE reduces the number of considered ellipses starting from a large, automatically defined set (the set CC of circles defined in the initialization step). Since there is no lower bound on the AIC as the number of ellipses decreases, this process continues until the set of all ellipses contains a single ellipse. In each iteration (each candidate number of ellipses from $|CC|$ down to 1), a pair of ellipses is selected as candidates for merging. DEFA considers the merging of adjacent ellipses, only. On the contrary, RFOVE considers any pair of ellipses as candidates for merging. The pair that is finally merged is the one that results in the lowest AIC. From all possible models (involving from a minimum of 1 to a maximum of $|CC|$ ellipses), RFOVE reports as its final solution the one with the minimum AIC.

3.2.5. Rejecting spurious solutions

For an ellipse E_i, we define its overlap ratio $O(E_i)$ as the percentage of its points that are overlapping with the union of the rest of the ellipses, that is:

$$O(E_i) = \frac{|E_i \cap (\bigcup j = 1, j \neq ikE_j)|}{|E_i|}. \quad (8)$$

An ellipse E_i with overlap $O(E_i)$ that is higher that a predefined threshold $T_{ov} = 95\%$ is rejected from being considered part of a model. Fig. 2 provides an example of such a situation. The ellipse E_2 has a high $O(E_2)$ value, therefore, a small contribution to the coverage of the image foreground, compared to a solution involving only E_1 and E_3. Thus, it can be excluded from the final solution.

Fig. 3 provides another example that shows that by setting appropriately the T_{ov} value, one can control the segmentation results. The figure shows the application of RFOVE in an image with $T_{ov} = 40\%$ (left, under-segmentation), and $T_{ov} = 95\%$ (right, near perfect segmentation).

RFOVE has the same computational complexity as DEFA [1]. This is equal to $O(c^2 n)$, where n denotes the number of foreground pixels and $c = |CC|$ denotes the number of circles that constitute the initial hypotheses of ellipses representing the 2D shape.

Fig. 4 illustrates an example run of RFOVE. Fig. 4 (a) shows the skeleton and the initial ellipse hypotheses of the 2D shape. Fig. 4 (b)–(f) show the ellipses estimated by RFOVE in the case of 9, 5, 3, 2 and 1 ellipses. The colormap of Fig. 4 (b)–(f)corresponds to $F(p)$, that is, the distance of foreground pixels from the ellipses introduced so far (cold and warm colors denote small and large distances, respectively). Fig. 4 (i) shows the final solution and the clustering of pixels ($\alpha_E = 98.8\%$), respectively. Fig. 4 (j) shows the AIC and BIC criteria for different values of k. A clear minimum at $k = 2$ is identified. As it can be verified, the minimization of AIC or BIC yields the same solution. Thanks to the ability of RFOVE to handle overlapping ellipses, this solution agrees with human intuition better than the solution of three ellipses provided by DEFA (Fig. 4 (g)) with $\alpha_E = 94.7\%$.

4. Using RFOVE for cell segmentation

We assume a gray-scale image (see Fig. 1 (a)) depicting a number of cells that vary with respect to size and shape and which may be touching each other. The cells as well as the background on which they appear may also vary in brightness. Each cell is free of holes and can be discriminated from its local background because of its higher brightness and its elliptic-like shape.

4.1. Segmenting cells from their background

The first step in our approach is to apply the Bradley's segmentation method [47] and a hole filling step. We get slightly better results by performing image smoothing, e.g. using a Gaussian filter with $\sigma = 2$, prior to segmentation. The Bradley's method calculates a locally adaptive image threshold that is chosen based on local, first-order image statistics around each pixel. This method is robust to illumination changes and clearly outperforms global thresholding techniques like Otsu's method [28] in images that exhibit strong illumination variations. A drawback of Bradley's method is that, segments of the background with locally higher brightness are identified erroneously as cells (see Fig. 5 (b)). To reduce these false positives, we have introduced two shape- and one appearance-based constraints.

- *Area constraint (shape):* The expected area of each cell should exceed a minimum threshold, T_α. So, segments that are particularly small, are rejected from further consideration. To avoid the rejection of cells that are partially visible (i.e., appear at/intersect with image boundaries), T_α is applied not to the measured object area but rather on an approximation of their *expected* area which is computed as the area of the circle that can be fitted best to the eight extrema points of their boundary [9].
- *Roundness constraint (shape):* Cells are circular/elliptic-like objects, so we have used the roundness measure to reject objects with complex shapes that deviate considerably from this pattern. The Roundness R measures how closely the shape of an object resembles that of a perfect circle and is defined by the following ratio:

$$R = \frac{4\pi\alpha}{p^2}, \quad (9)$$

where α and p denote the area and the perimeter of the object, respectively. The roundness R takes a maximum value of 1 for the perfect circle. According to our experiments, for a region to actually represent a cell it is required that $R > 0.2$.

- *Intensity constraint (appearance):* The aforementioned shape constraints suffice to reject several false positives as, for example, the one in the image center and the two in the top-right of Fig. 5 (b). We introduce another, intensity-based constraint, that is uncorrelated to the shape-based constraints, to reject more false positives such as the circular object on the top right of Fig. 5 (b). The intuition behind this constraint is that the intensity distribution within a cell should be more similar to the intensity distribution within the rest of the cells, rather than to the intensity distribution of the local background. To quantify this, we first extract the local background of each detected object by computing the Voronoi diagram of the objects' centroids and by removing from this the detected objects (see Fig. 5 (c)). To measure the distance between two intensity distributions, we employ the popular Bhattacharyya distance [51,52] under the assumption of normal distributions. More specifically, assuming two distributions q_1 and q_2, their

Fig. 2. (a) A 2D shape and (b) three ellipses E_1, E_2 and E_3 that are considered as a model approximating it. Notice that E_2 has very large overlap with E_1 and E_3 (yellow pixels), so it does not contribute significantly to increasing the coverage of the shape. Given that this overlap is greater than 95%, the proposed method will automatically reject the inclusion of this ellipse to the model of the 2D shape. (For interpretation of the references to color in this figure legend, the reader is referred to the web version of this article.)

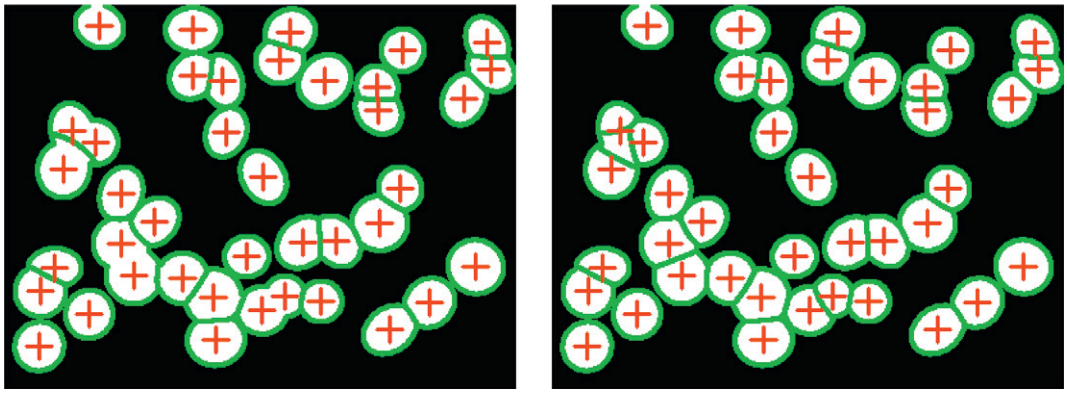

Fig. 3. (a) A solution of RFOVE with $T_{ov} = 40\%$ and (b) $T_{ov} = 95\%$.

means μ_i and their variances σ_i^2, $i \in \{1,2\}$, the Bhattacharyya distance $D(q_1,q_2)$ of q_1 and q_2 is defined as [53]:

$$D(q_1,q_2) = \frac{1}{4}\left[ln\left(\frac{\sigma_1^2}{4\sigma_2^2} + \frac{\sigma_2^2}{4\sigma_1^2} + \frac{1}{2}\right) + \frac{(\mu_1-\mu_2)^2}{\sigma_1^2+\sigma_2^2}\right]. \quad (10)$$

Fig. 5 (b) shows the boundaries of the detected cells as those were identified by the original Bradley's segmentation method [47] superimposed to the input image and the ground truth as in Fig. 1 (f) The four false positives are rejected by employing the proposed constraints (see Fig. 5 (d)).

4.2. Identifying overlapping cells

We apply RFOVE to each and every connected region that comes as a result of the previous segmentation step. In practice, assuming that most of the cells appear isolated (i.e. not overlapping with others), we apply RFOVE in all regions whose area is greater than the median area of all detected regions. This results in a computational speedup of about 50% without sacrificing the quality of the obtained results. If more that half of the connected components resulting from the segmentation step correspond to overlapping/touching cells, the median can be substituted by a lower percentile value.

5. Experimental evaluation

We performed several classes of experiments to evaluate quantitatively and qualitatively RFOVE[1] and its capacity to (a) approximate 2D shapes with ellipses and (b) to support the segmentation of potentially overlapping cells. The following sections describe the employed datasets (Section 5.1), the evaluation metrics used (Section 5.2) and the obtained results (Sections 5.3 and 5.4). In each experiment, RFOVE is compared quantitatively against state of the art approaches. Qualitative results are also provided.

5.1. The employed datasets

The experimental evaluation of the proposed method was conducted based on several datasets [54,18,1].

5.1.1. DEFA dataset [1]

This dataset contains 3950 binary shapes. It consists of the following four sub-datasets:

- MPEG-7 dataset [55]: consists of 1400 shapes organized in 70 categories with 20 shapes per category.
- a subset of LEMS [56], i.e., 1462 shapes that come from the following categories of the original database: Buildings,

[1] Our intention is to make the code implementing the proposed method together with the datasets and the experimental results publicly available at https://sites.google.com/site/costaspanagiotakis/research/cs.

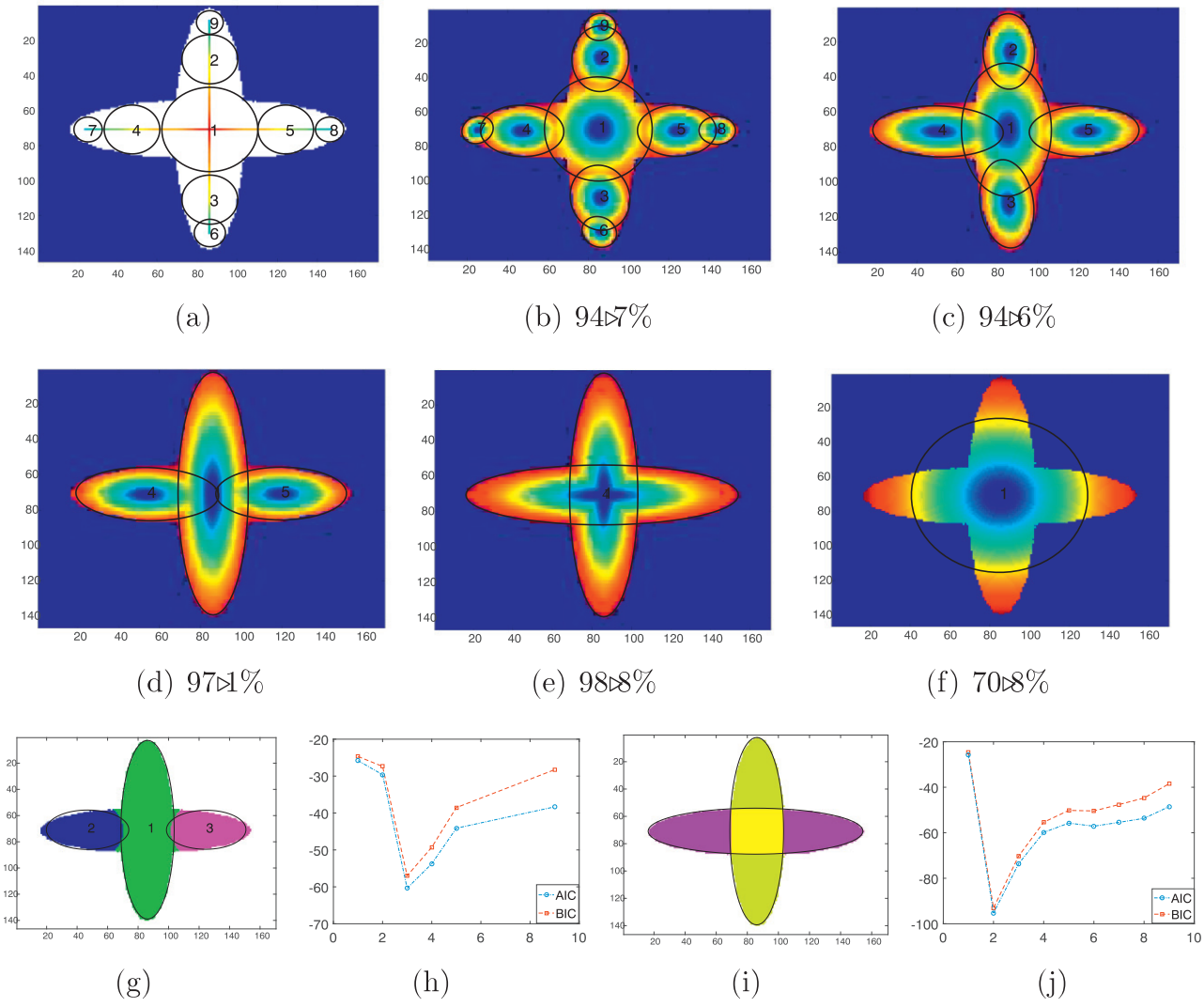

Fig. 4. (a) The skeleton and the initial ellipse hypotheses of the 2D shape. (b)–(f): The intermediate solutions proposed by RFOVE using 9, 5, 3, 2 and 1 ellipses. Captions show the estimated values of shape coverage α_E. (g) The association of pixels to $k = 3$ ellipses which is the final solution estimated by DEFA. (h) The AIC and BIC criteria for different values of k for DEFA. (i) The association of pixels to $k = 2$ ellipses which is the final solution estimated by RFOVE. The points in yellow color contribute to the definition of both ellipses. (j) The AIC and BIC criteria for different values of k for RFOVE. (For interpretation of the references to color in this figure legend, the reader is referred to the web version of this article.)

Containers, Fish, Fruit and vegetables, Misc Animal, People, Robots, Toddlers and Turtles, and SISHA SCALE and SISHA SHEAR datasets.

- SISHA SCALE dataset [1]: Contains 32 original shapes and 16 scale transformations (544 images in total).
- SISHA SHEAR dataset [1]: Contains 32 original shapes and 16 shear transformations (544 images in total).

5.1.2. U20S dataset [54]

A collection of 48 images (1349 × 1030 pixels) that include 1831 U20S cells.

5.1.3. NIH3T3 dataset [54]

A collection of 49 images (1344 × 1024 pixels) that include 2178 NIH3T3 cells. The NIH3T3 dataset is more challenging than U20S

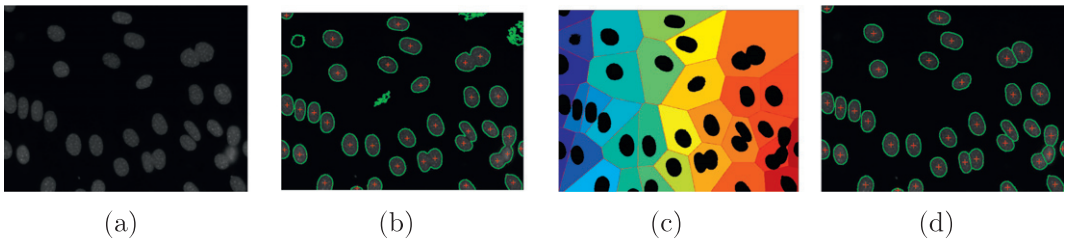

Fig. 5. (a) A fluorescence microscopy image. (b) The boundaries of the cells as detected by the Bradley's segmentation method [47] superimposed on (a). The ground truth cell centroids are shown with red "+". (c) The detected cells (plotted in black) and their local backgrounds defined based on the Voronoi diagram of their centroids. (d) The final cell segmentation result of the RFOVE method. (For interpretation of the references to color in this figure legend, the reader is referred to the web version of this article.)

Table 1
The average AIC of AEFA, DEFA and RFOVE, the $Pr(AEFA/AIC)$, $Pr(DEFA/AIC)$ and the $Pr(RFOV\,E/AIC)$ computed on all images of the four DEFA datasets.

Dataset	AIC AEFA	AIC DEFA	AIC RFOVE	Pr (AEFA/AIC)	Pr (DEFA/AIC)	Pr (RFOVE/AIC)
MPEG-7	−44.7	−45.1	**−49.5**	7.6%	9.1%	**71.2%**
LEMS	−63.5	−63.9	**−69.4**	3.8%	3.5%	**87.3%**
SISHA-SCALE	−43.6	−44.6	**−48.7**	6.4%	7.4%	**75.7%**
SISHA-SHEAR	−53.4	−54.3	**−59.4**	9.4%	10.3%	**75.4%**

Bold entries show the top-performing method.

dataset, since it contains cells/nuclei with varying brightness, and images often contain visible debris [54]. Both U20S and NIH3T3 datasets include cells that are heterogeneous in shape and size.

5.1.4. Synthetic dataset [18]

Consists of images with overlapping objects with elliptical shape that are randomly scaled, rotated, and translated. The dataset consists of 150 sample images of 300 × 400 pixels, split into three subsets based on the degree of overlap of the objects. In each subset the maximum overlap ratios allowed are 40%, 50%, and 60%, respectively. Each subset of images in the dataset contains 50 images of 40 objects. The minimum and maximum width and height of the bounding boxes of the ellipses are 30, and 45 pixels, respectively.

5.2. Evaluation criteria

Several metrics are used to evaluate RFOVE. The multitude of these metrics is because (a) we want to evaluate several different aspects of RFOVE, (b) different datasets provide ground truth in different forms and (c) in order to be able to compare with different state of the art methods and, given the lack of availability of their implementations, we need to adapt to the evaluation metrics used in the relevant publications.

5.2.1. Metrics for multi-ellipse fitting

Given the lack of objective ground truth in the DEFA dataset, as in [1], we compare multi-ellipse fitting methods on the basis of the shape coverage α_E and the AIC that they achieve. A larger shape coverage is preferable. Moreover, a smaller AIC signifies better balance between model complexity and shape coverage. To compare methods on the basis of a, we also compute $Pr(m/\alpha_E)$. For a given multi-ellipse fitting method m, $Pr(m/\alpha_E)$ is the percentage of images of the dataset in which method m *clearly outperforms* all other methods it is compared with respect to coverage α_E. As in [1], a method is supposed to clearly outperform another method if its performance in a certain metric is better by a margin of 0.1%. It also turns out that the value $100\% - \sum_m Pr(m/\alpha_E)$ gives the percentage of images of the dataset for which there is no clear winner method. As an example, the interpretation of the 6th column of the first line on Table 2 is that in the MPEG7 dataset, RFOVE clearly outperformed AEFA and DEFA in the coverage α_E criterion in 68.7% of the images. Similarly, we define and compute $Pr(m/AIC)$.

In datasets where ground truth is available (e.g., in Synthetic dataset), to assess the performance of ellipse fitting we employ

Table 2
The average coverage α_E of AEFA, DEFA and RFOVE, the $Pr(AEFA/\alpha_E)$, $Pr(DEFA/\alpha_E)$ and the $Pr(RFOV\,E/\alpha_E)$ computed on all images of the four DEFA datasets.

Dataset	α_E AEFA	α_E DEFA	α_E RFOVE	Pr (AEFA/α_E)	Pr (DEFA/α_E)	Pr (RFOVE/α_E)
MPEG-7	89.9%	90.1%	**91.7%**	8.4%	8.1%	**68.7%**
LEMS	93.0%	93.1%	**94.7%**	4.0%	3.9%	**84.4%**
SISHA-SCALE	93.6%	93.7%	**94.8%**	5.9%	5.1%	**74.4%**
SISHA-SHEAR	92.9%	93.0%	**94.5%**	7.5%	10.5%	**73.7%**

Bold entries show the top-performing method.

Table 3
Comparison of the performance of seedpoint extraction methods on the Synthetic dataset [18]. The second column shows the maximum overlap ratios of each of the three categories (40%, 50%, and 60%) of the Synthetic dataset.

	Overlap ratio in input [%]	TPR [%]	PPV [%]	AD (pixel)
BE-FRS [18]	40	95	**100**	2.03
FRS [43]	40	96	99	2.14
SBF [45]	40	**97**	97	2.85
DEFA [1]	40	76	87	0.81
RFOVE (proposed)	40	96	97	**0.58**
BE-FRS [18]	50	93	**100**	2.10
FRS [43]	50	**94**	97	2.20
SBF [45]	50	**94**	99	3.05
DEFA [1]	50	71	85	1.12
RFOVE (proposed)	50	91	95	**0.78**
BE-FRS [18]	60	92	**100**	2.23
FRS [43]	60	**94**	99	2.32
SBF [45]	60	**94**	96	3.08
DEFA [1]	60	68	86	1.53
RFOVE (proposed)	60	89	96	**1.04**

Bold entries show the top-performing method.

the True Positive Rate (TPR) and Positive Predictive Value (PPV), as in [18]:

$$TPR = \frac{TP}{TP + FN} \tag{11}$$

$$PPV = \frac{TP}{TP + FP}, \tag{12}$$

where True Positive (TP) is the number of correctly detected seedpoints or segmented objects, False Positive (FP) is the number of incorrectly detected seedpoints or segmentation results, and False Negative (FN) is the number of missed seedpoints of objects. For RFOVE, the equivalent of seedpoints are the centroids of the estimated ellipses. Similarly to [18], in order to determine whether a seedpoint was correctly detected (TP), the distance to the ground truth object center was computed and the decision was made using a predefined threshold. The threshold value was set to 8 pixels [18]. The average distance (AD) from detected seedpoints to the ground truth object center point was used as the third performance measure for seedpoint extraction. To decide whether the splitting result was correct or incorrect, the Jaccard Similarity coefficient (JSC) was used. The threshold values for the ratio of overlap were set 0.7 as in [18]. The average Jaccard Similarity coefficient ($AJSC$) value was also used as another metric for evaluating the splitting performance.

5.2.2. Metrics for cell segmentation

We employed both region-based and contour-based metrics, as in [19]. The region-based metrics include the JSC Similarity coefficient, widely used to measure spatial overlap, as well as Dice false

Table 4
Comparison of the performance of the proposed method on the Synthetic dataset [18]. The second column shows the maximum overlap ratios of each of the three categories (40%, 50%, and 60%) of the Synthetic dataset.

	Overlap ratio in input [%]	TPR [%]	PPV[%]	AJSC [%]
BE-FRS [18]	40	93	95	89
CECS [15]	40	89	91	83
DEFA [1]	40	72	83	86
RFOVE (proposed)	40	**95**	**96**	**92**
BE-FRS [18]	50	**88**	92	83
CECS [15]	50	82	87	73
DEFA	50	64	77	84
RFOVE (proposed)	50	82	**92**	**90**
BE-FRS [18]	60	**87**	**91**	80
CECS [15]	60	75	83	65
DEFA [1]	60	59	75	83
RFOVE (proposed)	60	84	**91**	**89**

Bold entries show the top-performing method.

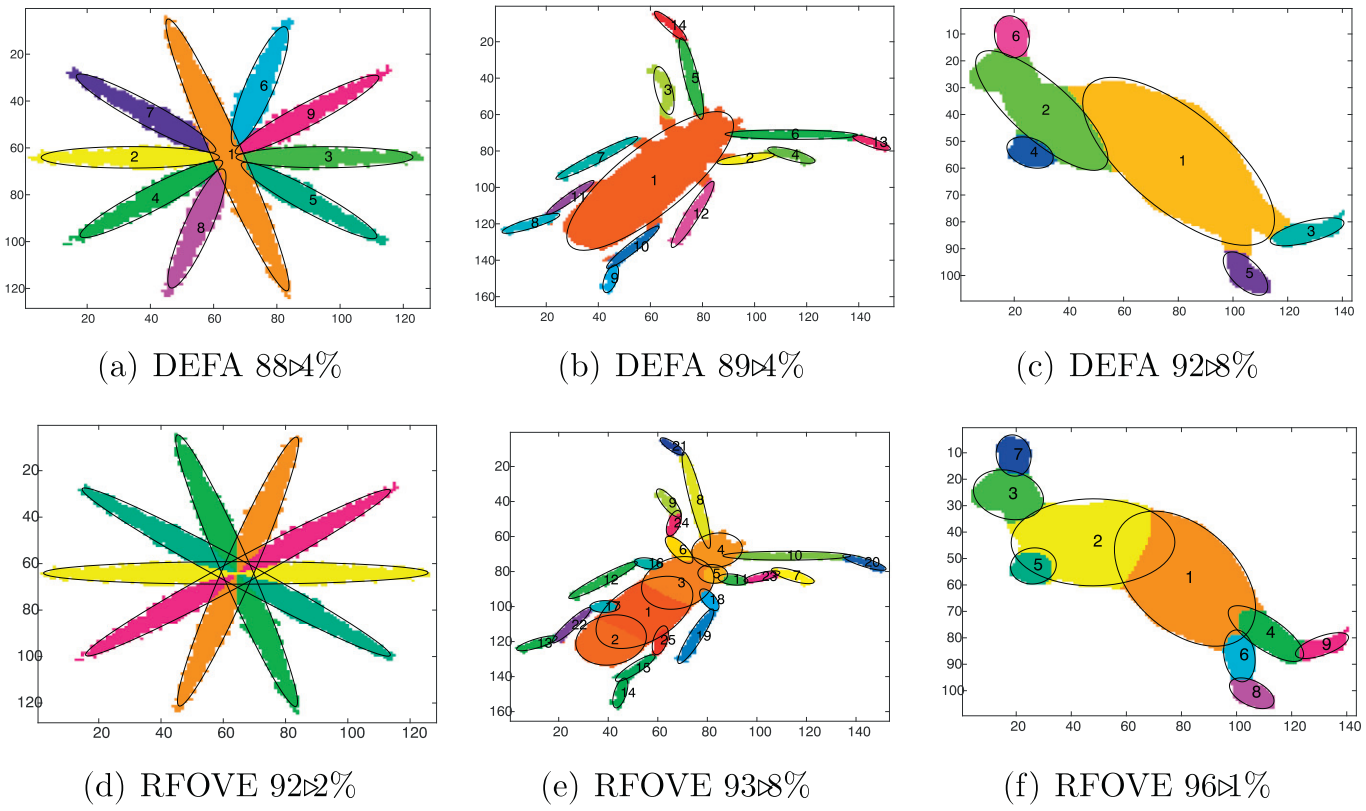

Fig. 6. Results of DEFA (1st row) and RFOVE (2nd row) on selected shapes from the LEMS dataset. Captions show the values of achieved shape coverage α_E.

positives (*Dice FP*) and Dice false negatives (*Dice FN*). *Dice FP* assesses over-segmentation and *Dice FN* under-segmentation. As contour-based metrics, we use the *Hausdorff* distance and the Mean Absolute contour Distance (*MAD*).

5.2.3. Metrics for cell splitting

As in [19], we also employ the number of false positives (*FP*) that counts the spuriously segmented cells and the number of false negatives (*FN*) that counts the cells that have not been segmented.

5.3. Results on multi-ellipse fitting

5.3.1. Quantitative results

We evaluated the capacity of RFOVE to perform multi-ellipse fitting on the DEFA dataset and in comparison with the AEFA and DEFA methods [1]. Table 1 shows the average AIC of AEFA, DEFA and RFOVE, as well as the *Pr*(*AEFA*/*AIC*), *Pr*(*DEFA*/*AIC*) and the *Pr*(*RFOV E*/*AIC*) computed in the four DEFA sub-datasets. The corresponding statistics for shape coverage α_E are presented in Table 2. RFOVE clearly outperforms AEFA and DEFA. DEFA slightly outperforms AEFA as also reported in [1]. When α_E is considered, RFOVE outperforms AEFA and DEFA in 78% of the 3950 shapes. When AIC is considered, RFOVE outperforms AEFA and DEFA in 80% of the 3950 shapes. RFOVE is clearly superior in the LEMS dataset, where it outperforms AEFA and DEFA in 87% and 84% of the 1462 shapes, respectively, when *Pr*(*AEFA*/*AIC*) and α_E are considered. This can be explained by the fact that the average complexity of shapes in LEMS is higher than that of MPEG and SISHA datasets [1]. Thus, in LEMS there exist more complex shapes that are better modeled and approximated by RFOVE.

The performance of the RFOVE has been also evaluated on the Synthetic dataset [18] and in comparison to state of the art seedpoint based extraction methods (Table 3, comparison with BE-FRS [18], FRS [43] and SBF [45]), as well as ellipse fitting methods (Table 4, comparison with BE-FRS [18], CECS [15] and DEFA [1]). Both Tables show the performances of BE-FRS, FRS, SBF and CECS as reported in [18]. In all cases, the performance of RFOVE is comparable or surpasses that of the state of the art, while it clearly outperforms the competing seedpoint extraction methods on the average distance (*AD*) metric.

It should be mentioned that RFOVE requires the setting of only a few parameters (three shape and area constraints to remove spurious solutions). In contrast, the top performing method *BE-FRS* requires setting several parameters concerning the type of structuring element that determines the erosion process, the number of erosion operations, the range of radii at which the FRS transform is computed, the Radial-Strictness that defines to what extent the radial symmetry-ness of features and the divergence weight factor [18].

5.3.2. Qualitative results

Figs. 6 and 7 show representative results from DEFA and RFOVE on selected shapes from the LEMS and MPEG7 datasets, respectively. RFOVE gives lower AIC and higher coverage than DEFA even with lower number of ellipses (see Figs. 6 (a) and (d), 7(b) and (e)). In addition, thanks to its capability to handle ellipses with considerable overlap, RFOVE better captures shape details than DEFA (see Figs. 6 (b) and (e), (c) and (f), 7(a) and (d), (c) and (f)).

Fig. 8 shows three representative results of RFOVE method on the Synthetic dataset using three sample images belonging in the three categories of the Synthetic dataset with 40% (left), 50% (middle) and 60% (right) overlapping ratios. The ground truth centroid of each object is shown with a red plus. The boundaries detected by the proposed method are plotted in green color and are in almost full agreement with the ground truth.

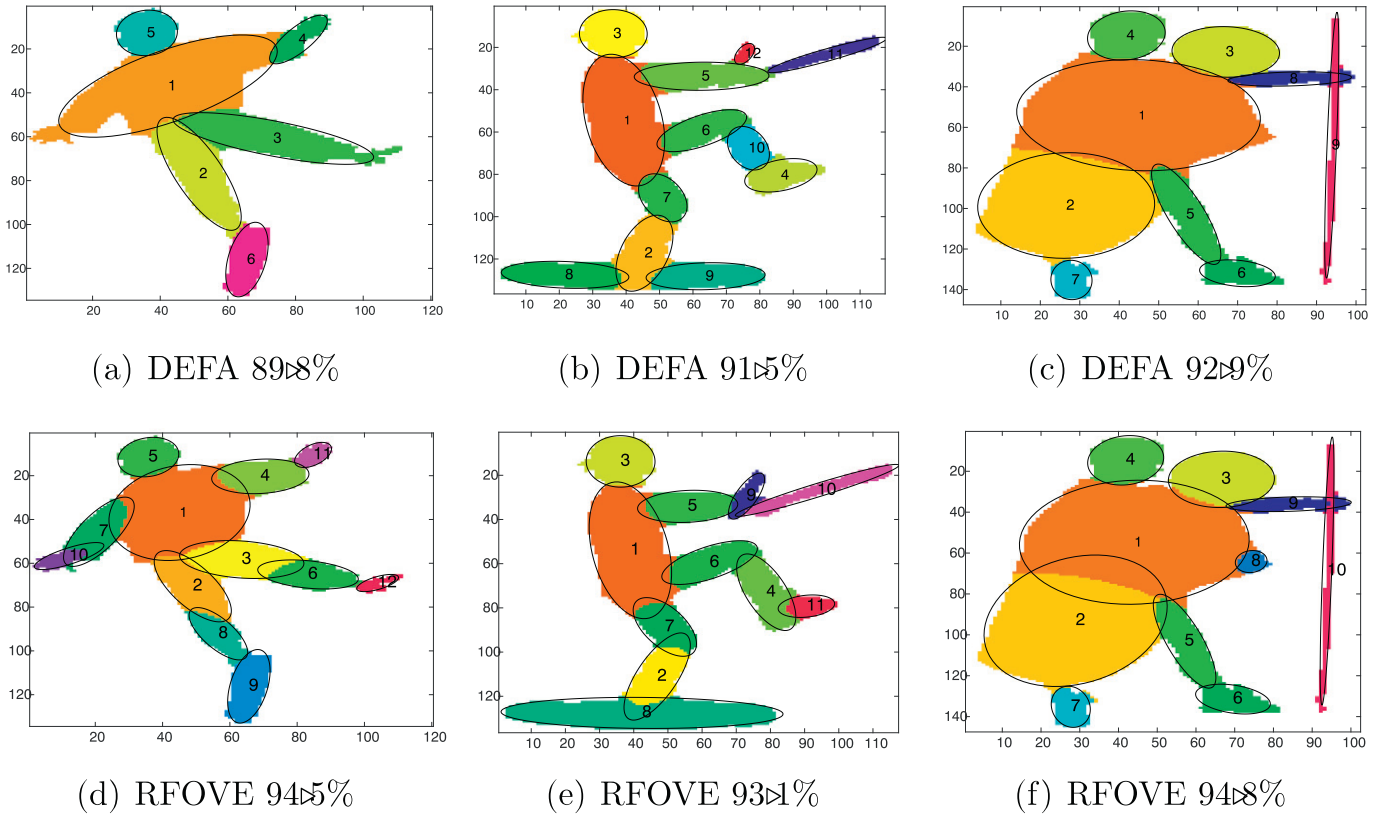

Fig. 7. Results of DEFA (1st row) and RFOVE (2nd row) on selected shapes from the MPEG7 dataset. Captions show the values of achieved shape coverage α_E.

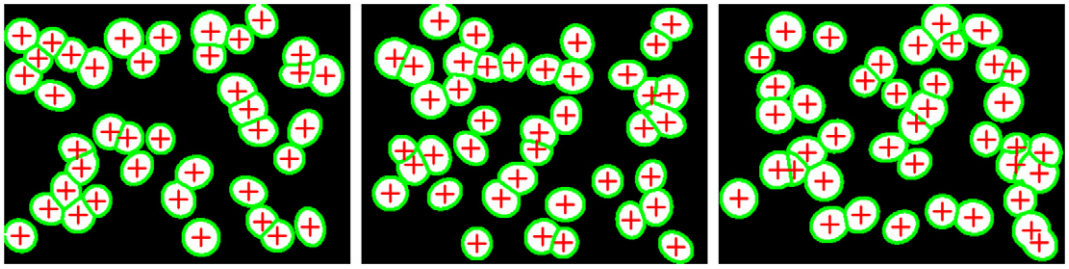

Fig. 8. Sample results of the RFOVE method on the Synthetic dataset [18]. The ground truth centroid of each object is shown with a red plus. The boundaries detected by the proposed method are plotted in green color. (For interpretation of the references to color in this figure legend, the reader is referred to the web version of this article.)

5.4. Results on cell segmentation/splitting

5.4.1. Quantitative results,comparison with non-learning-based methods

We evaluated the capacity of RFOVE to segment potentially overlapping cells with top performing non-learning-based methods, namely, the Three-step [32], the LSBR [31], the LLBWIP [19] and the Otsu method with a hole filling step as described in [13]. Tables 5 and 6 summarize the results obtained on the U20S and NIH3T3 datasets, respectively. Tables present average scores computed over individual scores per image of a dataset. On the U20S dataset, RFOVE and LLBWIP yield similar results, outperforming the rest of the methods. RFOVE clearly outperforms all the methods under any metric in the more challenging NIH3T3 dataset, due to the proposed adaptive image segmentation method that gives high performance results under variations on background and foreground brightness.

Table 7 gives the evaluation of splitting results on the U20S and NIH3T3 datasets, where the performances of the methods agree with the segmentation performances. This experiment shows that RFOVE outperforms the SEG-SELF method [46] reducing by about half the number of false positives *FP* in all dataset. SEG-SELF method differs from the proposed method in that it uses DEFA to identify splitting, instead of using RFOVE.

Table 5
Segmentation results on the **U20S** dataset.

Methods	JSC	MAD	Hausdorff	DiceFP	DiceFN
Otsu [13]	83.5	4.5	11.5	3.0	16.7
Three-step [32]	88.4	4.7	13.4	5.3	5.2
LSBR [31]	83.2	5.8	19.8	11.8	9.1
LLBWIP [19]	**91.6**	3.5	12.7	**4.7**	**3.9**
RFOVE (proposed)	89.8	**2.8**	**7.5**	5.2	5.7

Bold entries show the top-performing method.

Table 6
Segmentation results on the **NIH3T3** dataset.

Methods	JSC	MAD	Hausdorff	DiceFP	DiceFN
Otsu [13]	56.9	6.2	12.9	24.2	35.4
Three-step [32]	70.8	5.7	16.4	15.5	19.7
LSBR [31]	64.2	7.2	19.8	21.2	20.4
LLBWIP [19]	75.9	4.1	14.3	**12.7**	12.2
RFOVE (proposed)	**81.0**	**3.5**	**8.2**	13.3	**8.1**

Bold entries show the top-performing method.

Table 7
Splitting results on the **U20S** and **NIH3T3** datasets.

Methods	U20S		NIH3T3	
	FP	FN	FP	FN
Three-step [32]	0.5	3.9	1.7	11.3
LLBWIP [19]	**0.3**	2.7	1.5	5.0
SEG-SELF[46]	2.7	**0.3**	0.7	**0.8**
RFOVE (proposed)	1.9	**0.3**	**0.3**	**0.8**

Bold entries show the top-performing method.

5.4.2. Quantitative results,comparison with learning-based methods

A comparison of our unsupervised method to supervised, learning-based methods is not totally fair, however it is of practical interest to those working on the cell segmentation task. To perform such a comparison, we rely on the experimental results reported in [35,36] on the U20S and the NIH3T3 datasets that have been also employed in the current study. Deep learning methods [35] outperform the state of the art non-learning-based ones on cell segmentation. In [35], the reported *JSC* was 91.7% and was computed on the union of U20S and the NIH3T3 datasets, when half of them was used for training. The proposed RFOVE method that is the top performing non-learning-based method on this mixture of datasets yields 85.4%. The second top performing non-learning-based method was the LLBWIP [19] and yielded a *JSC* score of 83.8%.

Regarding the problem of cell splitting, according to the experimental results of [36], the proposed RFOVE method outperforms the proposed CNN 8 architecture that yields $FP = 1.3$ (split error) and $FN = 3.3$ (merge error) on U20S dataset and, $FP = 1.6$ (split error) and $FN = 4.1$ (merge error) on NIH3T3 dataset (see Table 7).

5.4.3. Qualitative results

Fig. 9 shows two representative results from the application of RFOVE on (a) the U20S and (b) the NIH3T3 dataset. In both cases, RFOVE successfully detects and correctly splits the high majority of cells, despite considerable variations in cell size, shape and intensity.

5.4.4. Computational time

In order to assess the computational efficiency of the proposed method and its applicability to medical imaging, we measured the computational time of both steps of the proposed method as function of image size (image area). We performed the running time experiments on a laptop with a Intel Core i7 2.2GHz processor and 32GB of RAM memory.

To study how the image size affects the computational time, the original images of a dataset have been cropped from the top right corner, according to three predefined percentages (25%, 50%, 75%) of the original image size. Then, the cropped images as well the original ones are used as input to the proposed method. Fig. 10 shows the average computational time from the application of the first (segmenting cells from their background) and the second (identifying overlapping cells) step of the proposed method to the NIH3T3 nucleus dataset as a function of the given image size. From this figure, it can be verified that computational time is linear to the image size. The first stage of the proposed method yields a segmentation output in 0.227 s on average in the original images of NIH3T3 nucleus dataset (1.38 MPixels). The corresponding computational time for the more time consuming stage of identifying the overlapping cells, is 24.4 s.

6. Summary and conclusions

We proposed RFOVE, a method that extends and improves DEFA [1] for approximating a 2D shape with an automatically defined number of ellipses. The key idea in this improvement was to allow for the consideration of ellipses with significant overlap. Extensive experiments on several datasets have shown that compared to DEFA, RFOVE approximates a given shape with increased shape coverage and with a better balance of shape coverage and model complexity. Towards a practical exploitation of the resulting algorithm, we employed RFOVE to the problem of segmenting potentially overlapping cells in fluorescence microscopy images. We showed that cell segmentation based on RFOVE outperforms cell segmentation based on DEFA. Moreover, the RFOVE-based segmentation method is comparable or even outperforms a number of competitive, state of the art methods on a variety of evaluation metrics and in a number of datasets. Ongoing work targets on the extensions of RFOVE towards handling shape primitives other than ellipses. In addition,

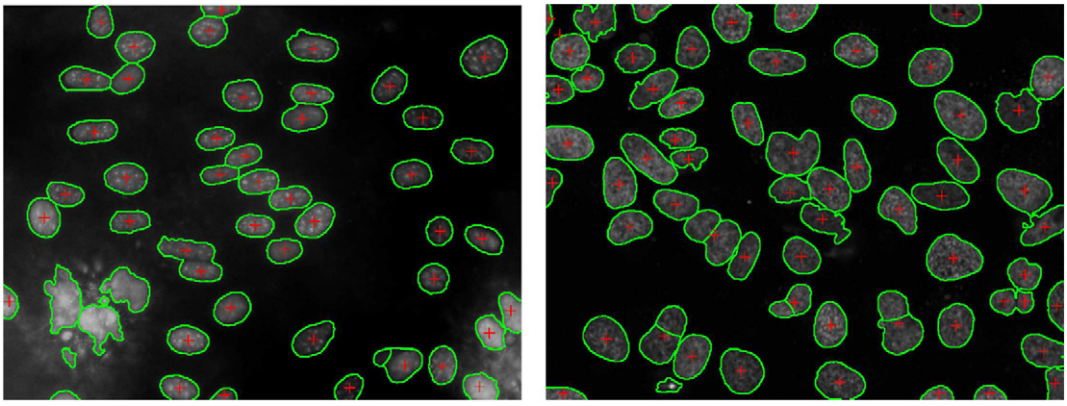

Fig. 9. Sample results of the RFOVE method on (a) the U20S and (b) the NIH3T3 datasets.

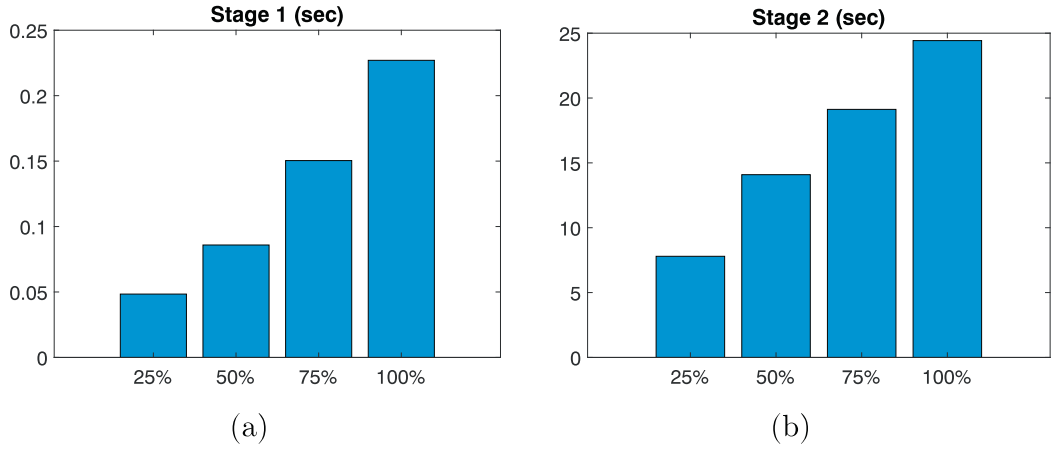

Fig. 10. Average computational time in seconds from the application of (a) the cell segmentation and (b) the overlapping cells identification steps of the proposed method on the NIH3T3 nucleus dataset as a function of the percentage of the original image size.

the extension of RFOVE to model 3D shapes can be considered as future work.

Declaration of competing interest

We wish to confirm that there are no known conflicts of interest associated with this publication and there has been no significant financial support for this work that could have influenced its outcome. We confirm that the manuscript has been read and approved by all named authors and that there are no other persons who satisfied the criteria for authorship but are not listed.

References

[1] C. Panagiotakis, A. Argyros, Parameter-free modelling of 2D shapes with ellipses, Pattern Recog. 53 (2016) 259–275.
[2] N.H. Trinh, B.B. Kimia, Skeleton search: category-specific object recognition and segmentation using a skeletal shape model, Int. J. Comput. Vis. 94 (2) (2011) 215–240.
[3] A. Toshev, B. Taskar, K. Daniilidis, Shape-based object detection via boundary structure segmentation, Int. J. Comput. Vis. 99 (2) (2012) 123–146.
[4] N. Kyriazis, A. Argyros, Scalable 3D tracking of multiple interacting objects, Proceedings of the IEEE Conference on Computer Vision and Pattern Recognition, 2013. pp. 3430–3437.
[5] C. Panagiotakis, E. Ramasso, G. Tziritas, M. Rombaut, D. Pellerin, Shape-based individual/group detection for sport videos categorization, Int. J. Pattern Recognit. Artif. Intell. 22 (06) (2008) 1187–1213.
[6] X. Ben, W. Meng, R. Yan, Dual-ellipse fitting approach for robust gait periodicity detection, Neurocomputing 79 (2012) 173–178.
[7] C. Panagiotakis, G. Tziritas, Any dimension polygonal approximation based on equal errors principle, Pattern Recogn. Lett. 28 (5) (2007) 582–591.
[8] X. Yang, X. Gao, D. Tao, X. Li, J. Li, An efficient MRF embedded level set method for image segmentation, IEEE Trans. Image Process. 24 (1) (2015) 9–21.
[9] I. Kåsa, A circle fitting procedure and its error analysis, IEEE Trans. Instrum. Meas. 1001 (1) (1976) 8–14.
[10] A. Levinshtein, E. Phung, P. Aarabi, Hybrid eye center localization using cascaded regression and hand-crafted model fitting, Image Vis. Comput. 71 (2018) 17–24.
[11] Q. Ji, 3D face pose estimation and tracking from a monocular camera, Image Vis. Comput. 20 (7) (2002) 499–511.
[12] W. Zhang, H. Li, Automated segmentation of overlapped nuclei using concave point detection and segment grouping, Pattern Recog. 71 (2017) 349–360.
[13] M. Liao, Y.-q. Zhao, X.-h. Li, P.-s. Dai, X.-w. Xu, J.-k. Zhang, B.-j. Zou, Automatic segmentation for cell images based on bottleneck detection and ellipse fitting, Neurocomputing 173 (2016) 615–622.
[14] X. Bai, C. Sun, F. Zhou, Splitting touching cells based on concave points and ellipse fitting, Pattern Recog. 42 (11) (2009) 2434–2446.
[15] W.-H. Zhang, X. Jiang, Y.-M. Liu, A method for recognizing overlapping elliptical bubbles in bubble image, Pattern Recognition Letters 33 (12) (2012) 1543–1548.
[16] A. Leonardis, A. Jaklic, F. Solina, Superquadrics for segmenting and modeling range data, IEEE Trans. Pattern. Anal. Mach. Intell. 19 (11) (1997) 1289–1295.
[17] C. Goldfeder, P.K. Allen, C. Lackner, R. Pelossof, Grasp planning via decomposition trees, Robotics and Automation, 2007 IEEE International Conference on, IEEE. 2007, pp. 4679–4684.
[18] S. Zafari, T. Eerola, J. Sampo, H. Kälviäinen, H. Haario, Segmentation of overlapping elliptical objects in silhouette images, IEEE Trans. Image Process. 24 (12) (2015) 5942–5952.
[19] A. Gharipour, A.W.-C. Liew, Segmentation of cell nuclei in fluorescence microscopy images: an integrated framework using level set segmentation and touching-cell splitting, Pattern Recog. 58 (2016) 1–11.
[20] S.-C. Zhang, Z.-Q. Liu, A robust, real-time ellipse detector, Pattern Recognit. 38 (2) (2005) 273–287.
[21] J. Yao, N. Kharma, P. Grogono, A multi-population genetic algorithm for robust and fast ellipse detection, Pattern Anal. Appl. 8 (1-2) (2005) 149–162.
[22] F. Mai, Y. Hung, H. Zhong, W. Sze, A hierarchical approach for fast and robust ellipse extraction, Pattern Recognit. 41 (8) (2008) 2512–2524.
[23] L. Rocha, L. Velho, P.C.P. Carvalho, Image moments-based structuring and tracking of objects, Computer Graphics and Image Processing, 2002. Proceedings. XV Brazilian Symposium on, IEEE. 2002, pp. 99–105.
[24] R.Y. Da Xu, M. Kemp, Fitting multiple connected ellipses to an image silhouette hierarchically, IEEE Trans. Image Process. 19 (7) (2010) 1673–1682.
[25] A. Wong, B. Taylor, A. Yuille, Exploiting protrusion cues for fast and effective shape modeling via ellipses, BMVC, 2017.
[26] C. Panagiotakis, I. Grinias, G. Tziritas, Natural image segmentation based on tree equipartition, bayesian flooding and region merging, IEEE Trans. Image Process. 20 (8) (2011) 2276–2287.
[27] C. Panagiotakis, H. Papadakis, E. Grinias, N. Komodakis, P. Fragopoulou, G. Tziritas, Interactive image segmentation based on synthetic graph coordinates, Pattern Recognit. 46 (11) (2013) 2940–2952.
[28] N. Otsu, A threshold selection method from gray-level histograms, IEEE Trans. Syst. Man Cybern. 9 (1) (1979) 62–66.
[29] H. Su, F. Xing, J.D. Lee, C.A. Peterson, L. Yang, Automatic myonuclear detection in isolated single muscle fibers using robust ellipse fitting and sparse representation, IEEE/ACM Trans. Comput. Biol.Bioinforma. (TCBB) 11 (4) (2014) 714–726.
[30] C. Panagiotakis, E. Ramasso, G. Tziritas, Lymphocyte segmentation using the transferable belief model, Recognizing Patterns in Signals, Speech, Images and Videos, Springer. 2010, pp. 253–262.
[31] Y.-T. Chen, A level set method based on the Bayesian risk for medical image segmentation, Pattern Recognit. 43 (11) (2010) 3699–3711.
[32] J.-P. Bergeest, K. Rohr, Efficient globally optimal segmentation of cells in fluorescence microscopy images using level sets and convex energy functionals, Med. Image Anal. 16 (7) (2012) 1436–1444.
[33] J. Wang, J.D. MacKenzie, R. Ramachandran, D.Z. Chen, Neutrophils identification by deep learning and voronoi diagram of clusters, International Conference on Medical Image Computing and Computer-Assisted Intervention, Springer. 2015, pp. 226–233.
[34] Y. Song, E.-L. Tan, X. Jiang, J.-Z. Cheng, D. Ni, S. Chen, B. Lei, T. Wang, Accurate cervical cell segmentation from overlapping clumps in pap smear images, IEEE Trans. Med. Imaging 36 (1) (2017) 288–300.
[35] N. Ibtehaz, M.S. Rahman, MultiResUNet: Rethinking the U-Net Architecture for Multimodal Biomedical Image Segmentation, arXiv preprint. (2019) arXiv: 1902.04049.
[36] J.Y. Huang, N.J. Hughes, G.J. Goodhill, Segmenting neuronal growth cones using deep convolutional neural networks, 2016 International Conference on Digital Image Computing: Techniques and Applications (DICTA), IEEE. 2016, pp. 1–7.
[37] T. He, H. Mao, J. Guo, Z. Yi, Cell tracking using deep neural networks with multi-task learning, Image Vis. Comput. 60 (2017) 142–153.
[38] O. Ronneberger, P. Fischer, T. Brox, U-net: convolutional networks for biomedical image segmentation, International Conference on Medical image computing and computer-assisted intervention, Springer. 2015, pp. 234–241.
[39] C. Wählby, J. Lindblad, M. Vondrus, E. Bengtsson, L. Björkesten, Algorithms for cytoplasm segmentation of fluorescence labelled cells, Analytical Cellular Pathology 24 (2-3) (2002) 101–111.

[40] C. Jung, C. Kim, Segmenting clustered nuclei using H-minima transform-based marker extraction and contour parameterization, IEEE Trans. Biomed. Eng. 57 (10) (2010) 2600–2604.
[41] A. Fitzgibbon, M. Pilu, R.B. Fisher, Direct least square fitting of ellipses, IEEE Trans. Pattern Anal. Mach. Intell. 21 (5) (1999) 476–480.
[42] C. Park, J.Z. Huang, J.X. Ji, Y. Ding, Segmentation, inference and classification of partially overlapping nanoparticles, IEEE Trans. Pattern Anal. Mach. Intell. 35 (3). (2013)1-1.
[43] G. Loy, A. Zelinsky, Fast radial symmetry for detecting points of interest, IEEE Trans. Pattern Anal. Mach. Intell. 25 (8) (2003) 959–973.
[44] M. Fornaciari, A. Prati, R. Cucchiara, A fast and effective ellipse detector for embedded vision applications, Pattern Recognit. 47 (11) (2014) 3693–3708.
[45] C.S. Pereira, H. Fernandes, A.M. Mendonça, A. Campilho, Detection of lung nodule candidates in chest radiographs, Iberian Conference on Pattern Recognition and Image Analysis, Springer. 2007, pp. 170–177.
[46] C. Panagiotakis, A.A. Argyros, Cell segmentation via region-based ellipse fitting, 2018 25th IEEE International Conference on Image Processing (ICIP), IEEE. 2018, pp. 2426–2430.
[47] D. Bradley, G. Roth, Adaptive thresholding using the integral image, J. Graph. Tools 12 (2) (2007) 13–21.
[48] H. Akaike, A new look at the statistical model identification, IEEE Trans. Autom. Control. 19 (6) (1974) 716–723.
[49] L. Lam, S.-W. Lee, C.Y. Suen, Thinning methodologies-a comprehensive survey, IEEE Trans. Pattern. Anal. Mach.Intell. 14 (9) (1992) 869–885.
[50] A.K. Jain, Fundamentals of Digital Image Processing, Prentice-Hall, Inc.. 1989.
[51] E. Choi, C. Lee, Feature extraction based on the Bhattacharyya distance, Pattern Recognit. 36 (8) (2003) 1703–1709.
[52] S. Liapis, G. Tziritas, Color and texture image retrieval using chromaticity histograms and wavelet frames, IEEE Trans. Multimed. 6 (5) (2004) 676–686.
[53] G.B. Coleman, H.C. Andrews, Image segmentation by clustering, Proc. IEEE 67 (5) (1979) 773–785.
[54] L.P. Coelho, A. Shariff, R.F. Murphy, Nuclear segmentation in microscope cell images: a hand-segmented dataset and comparison of algorithms, Proceedings - 2009 IEEE International Symposium on Biomedical Imaging: From Nano to Macro, ISBI 2009, 2009.
[55] L.J. Latecki, R. Lakamper, T. Eckhardt, Shape descriptors for non-rigid shapes with a single closed contour, IEEE Conf. Comput. Vis. Pattern Recognit., vol. 1, IEEE. 2000, pp. 424–429.
[56] B. Kimia, A Large Binary Image Database, LEMS Vision Group at Brown University, 2002, http://www.lems.brown.edu/dmc/.